Electronic Supporting Information (ESI)

Recognizing nitroimidazole from nitrofuran via luminescence sensing

Wanyu Qi [a], Zicheng Wang [a], Xin Tong [a], Haibo Zhang[b*], Yuxin Li[a*]

[a]*Key Laboratory of Function Inorganic Material Chemistry (MOE), School of Chemistry and Material Science, Heilongjiang University, Harbin 150080, China.*

[b]*College of Chemistry and Molecular Sciences, Wuhan University, Wuhan 430072, China.*

Content

1. Experimental section

1.1 Chemicals and instrumentation

1.2 Synthesis of RhB@Tb-BPDC

1.3 Luminescent sensing methodology

1.4 Theoretical Calculation

2. Results and discussion

2.1 Structure characterization

2.2 Luminescent properties

2.3 Luminescent sensing toward NM antibiotics in water

2.4 Stability and Biotoxicity

3. Reference

1. Experimental section

1.1 Chemicals and Instrumentation

All chemicals and reagents were purchased from HWRK CHEMICALS without further purification. Powder X-ray diffraction (PXRD) patterns were tested by a Rigaku D/Max-3B X-ray diffractometer under Cu Kα (λ = 1.5406 Å) radiation and a graphite monochromator ranged from 5 º to 30 º. The thermogravimetric analysis (TGA) was performed by a PerkinElmer STA 6000 under air atmosphere with a 10 ℃/min heating rate from room temperature to 800 ℃. The UV-vis absorption spectra were recorded by using a PerkinElmer Lambda 35 spectrophotometer with the range of 200−700 nm. Fourier-transform infrared (FT-IR) spectra were recorded on a PerkinElmer Spectrum 100 spectrophotometer in 4000−500 cm^{-1} by using KBr as the diluent. The photoluminescence spectra were recorded by utilizing a FLS 1000 Edinburgh fluorescence spectrometer and a PerkinElmer FL 6500 spectrophotometer. Luminescence lifetimes were measured at room temperature on a single photon counting spectrometer with a microsecond pulse lamp as the excitation. The quantum yields of the complexes were determined at room temperature through a relative method using an Edinburgh Instruments integrating sphere coupled to the modular Edinburgh FLS 920 fluorescence spectrophotometer. The values reported are the average of five independent determinations for each sample. The quantum yield was measured on an integrating sphere measurement by using $[Ru(bpy)_3Cl_2]$ as a reference.[1]

1.2 Synthesis of RhB@Tb-BPDC

In a beaker containing 12 mL of a H_2O-DMF (1:4) mixed solvent, Tb $(NO_3)_3 \cdot 6H_2O$ (0.20 mmol), biphenyl-4,4'-dicarboxylic acid (0.5 mmol), and RhB were added. The mixture was stirred with a magnetic stirrer for 60 minutes. The solution was then transferred to a 25 mL Teflon-lined stainless-steel autoclave, sealed, and heated at 140°C for 72 hours. After heating, it was cooled gradually to room temperature at a rate of 0.1°C/min. Light pink crystals were collected by filtration, washed with ethanol and water, and air-dried. The yield was 65%.

1.3 Luminescent sensing methodology

At room temperature, 200 mg of RhB@Tb-BPDC composites were uniformly dispersed in 200 mL of distilled water. A 1 g/L suspension was then prepared by ultrasonication at 720 W for 1 hour.

For the selectivity experiment, 1 mL of the RhB@Tb-BPDC aqueous suspension prepared earlier was combined with 1 mL of a 10 mmol solution containing the corresponding antibiotics (DTZ, ODZ, NFZ, NFT, SMZ, CFD, KNM, THZ, DCL, ACL). After thorough mixing, the luminescence spectrum was measured. Luminescence was documented both before and after the addition of the analytes. Each experiment was replicated at least three times.

For the sensitivity assay: luminescence titration analyses of cations were executed by incrementally adding antibiotics. Consistent outcomes were observed. The limit of detection (LOD) was determined using the formula LOD =3σ/Ksv, where σ represents the standard deviation from three sets of luminescent readings of the control sample. The average σ value for antibiotics is 0.0099. This specific σ value can be derived using the equation σ = sqrt (((I_1 - I)^2 + (I_2 - I)^2 + (I_3 - I)^2)/3). The Stern-Volmer constant (*Ksv*) was extrapolated using the Stern-Volmer (SV) equation: lg(I_0/I - 1) = lg(Ksv) + n×lg [C].

In the competitive assay, a 1 mL sample of a 1 g/L RhB@Tb-BPDC aqueous suspension was combined with 25μL of the NFZ solution. The luminescence intensity at 545 nm was measured both before and after mixing, under an excitation wavelength of 312 nm ultraviolet light. Subsequently, 1 mL of a 10 mmol nitroimidazole solution was incrementally added, and the luminescence intensity was recorded after each addition.

In cyclic experiments, the spent RhB@Tb-BPDC aqueous suspension was centrifuged at a low temperature to separate the solid from the liquid. After decanting the supernatant, the residue was washed multiple times with water. The solid material was then thoroughly dried in a vacuum oven at 80°C. This dried powder can be repurposed as a sensor for both DTZ and ODZ. The sequence of detection, washing, drying, and redetection was repeated until the luminescence intensity at 545 nm declined to approximately 80% of the initial blank sample's intensity, signaling the end of the cyclic experiment.

1.4 Theoretical Calculation

Molecule optimized geometries and frontier molecular orbitals energies were performed using the Gaussian 16 package. Topologies of the frontier molecular orbitals have been extracted using Gaussview 6.0 graphical interface program. Molecular geometries were first optimized using the B3LYP method with the 6-311G* basis set. Then a single point energy calculation was performed at B3LYP/6-311+G(d,p) level of theory to extract the energies of the frontier molecular orbitals and the HOMO-LUMO gap presented at Fig.3a in the main text, Optimized geometries were also obtained at B3LYP/6-311+G(d,p) level of theory. In no case, symmetry constraints were imposed, and all the optimized structures were verified as a stationary point, by harmonic vibrational frequency calculation (no imaginary frequencies) at the same level of theory as in optimizations.

2. Results and discussion.

2.1 Structure characterization.

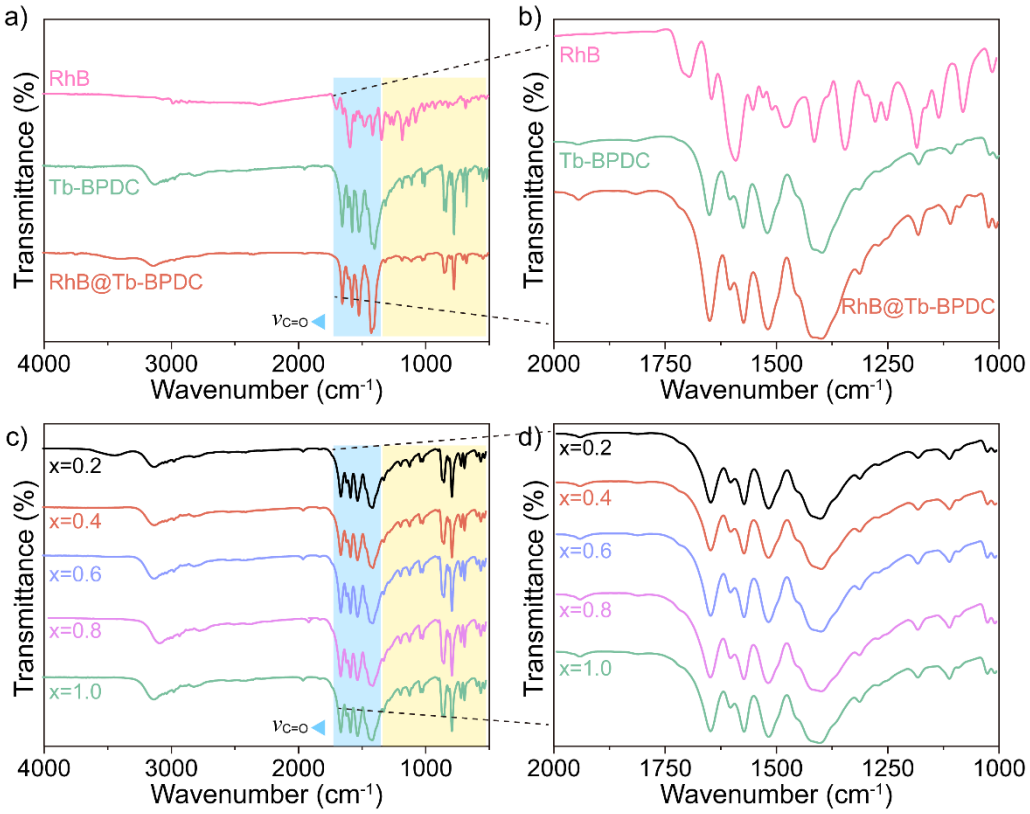

Fig. S1. (a) and (b) FT-IR spectra of RhB, Tb-BPDC and RhB@Tb-BPDC; (c) and (d) FT-IR spectra of $RhB_{0.2}$@Tb-BPDC, $RhB_{0.4}$@Tb-BPDC, $RhB_{0.6}$@Tb-BPDC, $RhB_{0.8}$@Tb-BPDC and $RhB_{1.0}$@Tb-BPDC.

Between 1400 and 1650 (cm^{-1}), one can identify four sharp, well-defined absorption peaks, primarily attributed to the vibrational stretching of the carbonyl $(C=O)_2$ groups present in the $BPDC^{2-}$ ligands' carboxylate sections. Additionally, a prominent, sharp peak around 770 (cm^{-1}) is observed, typically associated with the C–H bending vibrations in 1,4-disubstituted aromatic compounds. Following the encapsulation of dye molecules, the vibrational modes of the bonds, especially those below 1600 (cm^{-1}), exhibit noticeable dampening.[2] This reduction in vibrational activity is mainly due to the encapsulation process, which imposes increased rigidity on the dye molecules. The confinement within a host matrix limits the dye molecules' mobility, resulting in

diminished vibrational movement. Therefore, the reduced vibrational activity serves as a strong indication of successful encapsulation, signifying the immobilization and maintained structural integrity of the dye molecules in their new setting.

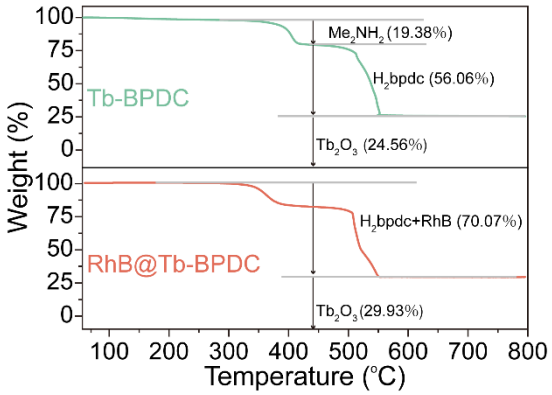

Fig. S2. TGA curves of Tb-BPDC and RhB@Tb-BPDC.

The revision highlights the material's significant thermal stability up to 300°C and the initial weight loss due to the desorption of protonated dimethylamine molecules. It further clarifies that at 480°C, the material begins to collapse, marking the critical point of framework stability, followed by a decomposition process leading to the final residue of Tb_2O_3. RhB starts to decompose in the 290-350°C range, reflecting the specific thermal instability of the RhB-BPDC ligand complex. During decomposition, RhB's organic components undergo thermal breakdown along with the simultaneous decomposition of BPDC ligands. This detailed step highlights the complexity and sequence of interactions among the components of the composite material during the thermal decomposition process. Ultimately, this decomposition leads to the complete transformation of all organic components, leaving Tb_2O_3 as the residual solid.

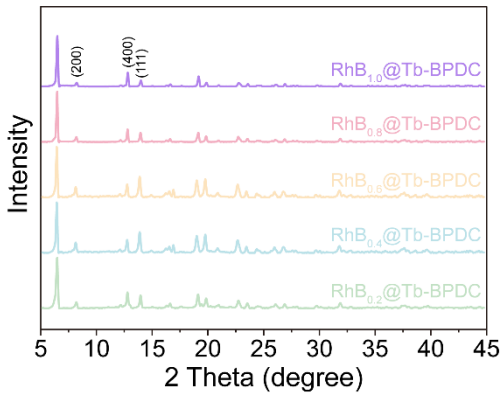

Fig. S3. PXRD patterns of $RhB_{0.2}$@Tb-BPDC, $RhB_{0.4}$@Tb-BPDC, $RhB_{0.6}$@Tb-BPDC, $RhB_{0.8}$@Tb-BPDC and $RhB_{1.0}$@Tb-BPDC.

2.2 Luminescent properties

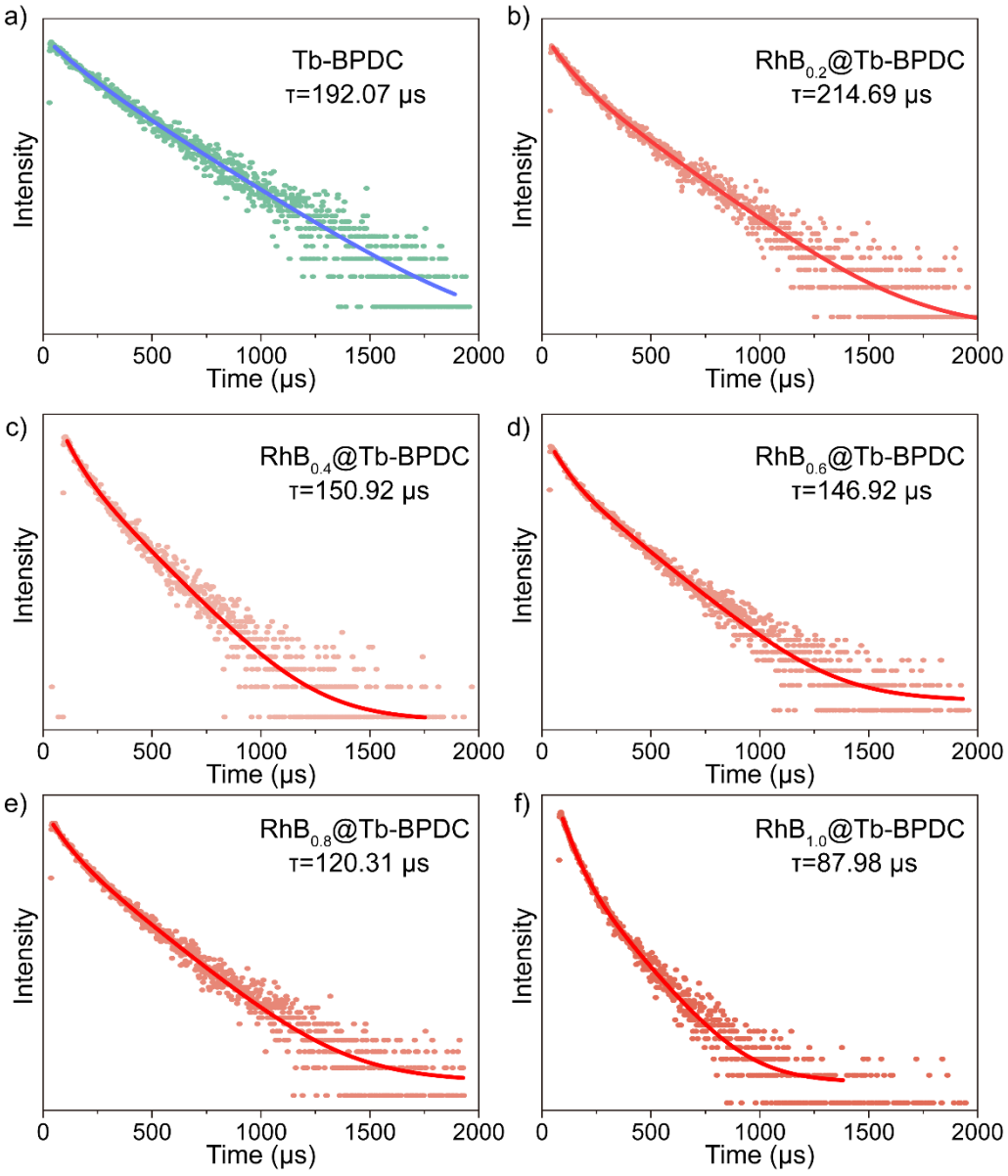

Fig. S4. Luminescent lifetimes of solid-state Tb-BPDC, $RhB_{0.2}$@Tb-BPDC, $RhB_{0.4}$@Tb-BPDC, $RhB_{0.6}$@Tb-BPDC, $RhB_{0.8}$@Tb-BPDC and $RhB_{1.0}$@Tb-BPDC.

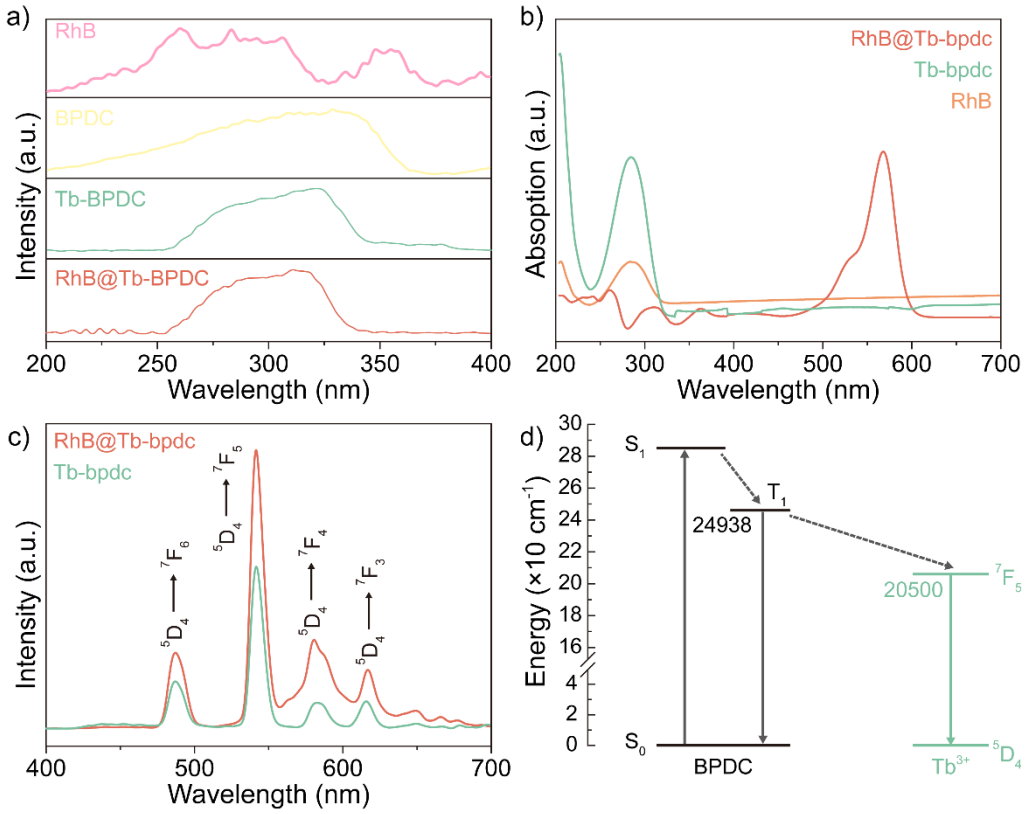

Fig. S5. (a) Excitation spectra of RhB, BPDC, Tb-BPDC, RhB@Tb-BPDC; (b) UV−Vis spectra of Tb-BPDC, RhB, and RhB@Tb-BPDC; (c) luminescence intensity of Tb-BPDC and RhB@Tb-BPDC; (d) The energy transfer from BPDC ligands to Tb^{3+}.[3]

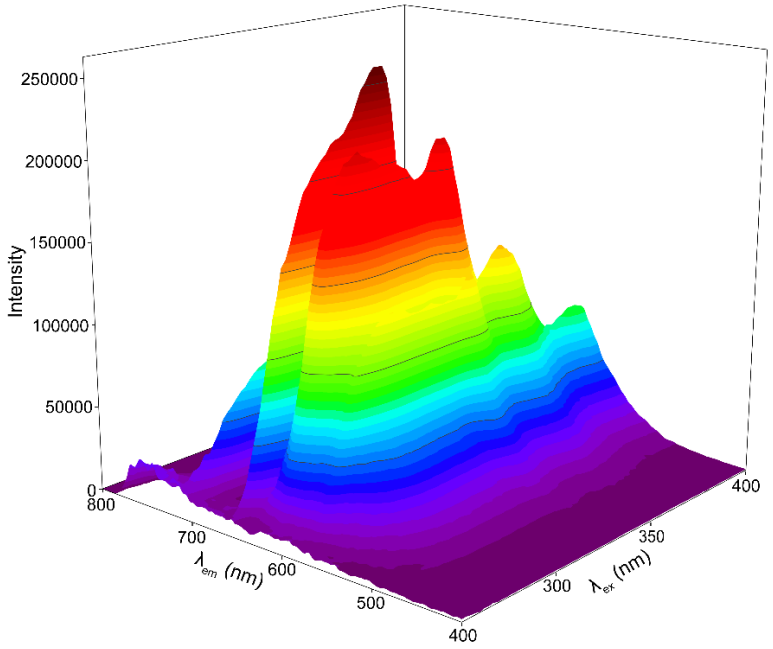

Fig. S6. Three-dimensional photoluminescence spectrum of solid-state RhB@Tb-BPDC.

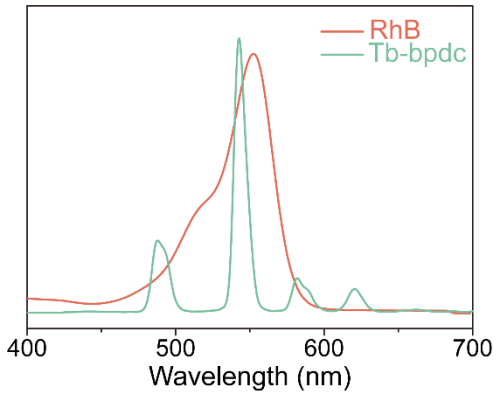

Fig. S7. Spectral overlap between the absorption of RhB and the emission of Tb-BPDC

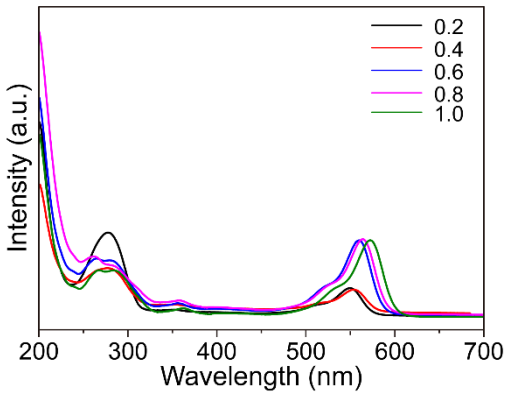

Fig. S8. Absorption spectra of Tb-BPDC containing different concentrations of RhB.

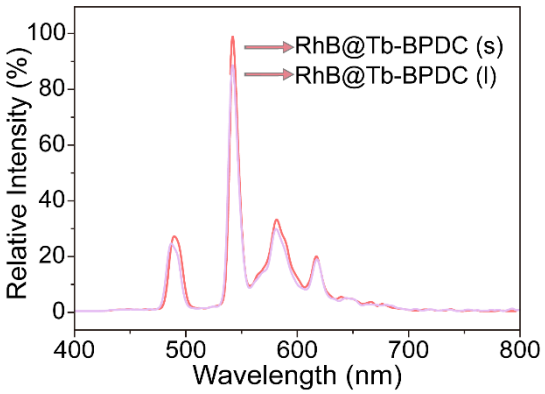

Fig. S9. Photoluminescence spectra of RhB@Tb-BPDC solid and 1 g/L RhB@Tb-BPDC aqueous suspension.

2.3 Luminescent sensing toward nitroimidazole antibiotics in water

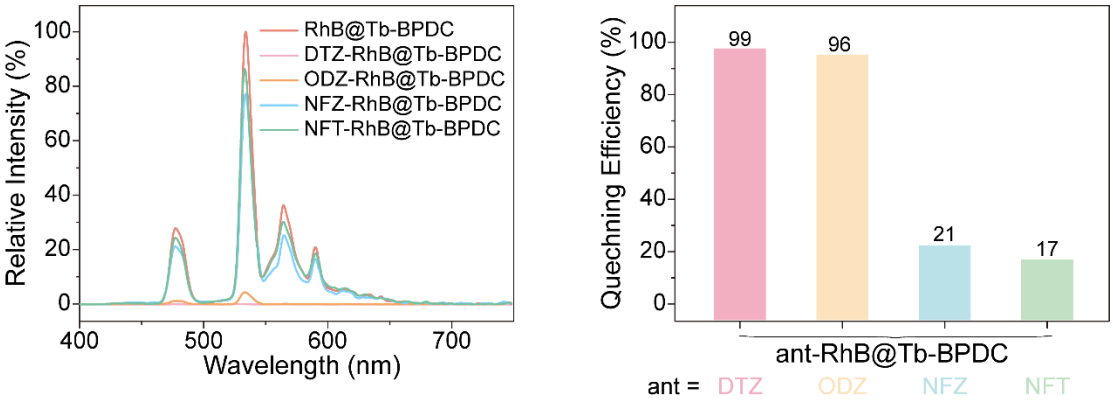

Fig. S10. Quenching efficiency of RhB@Tb-BPDC after adding ODZ, DTZ, NFZ and NFT.

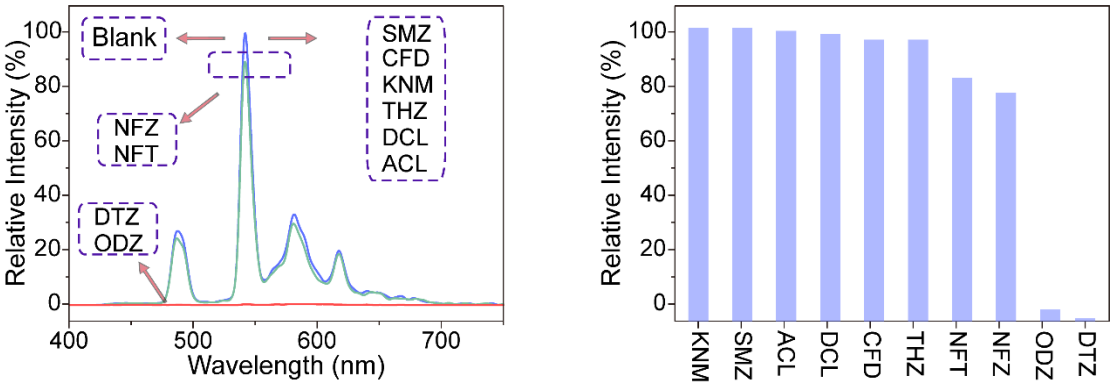

Fig. S11. Luminescence spectra of RhB@Tb-BPDC aqueous solution in the absence and presence of various antibiotics.

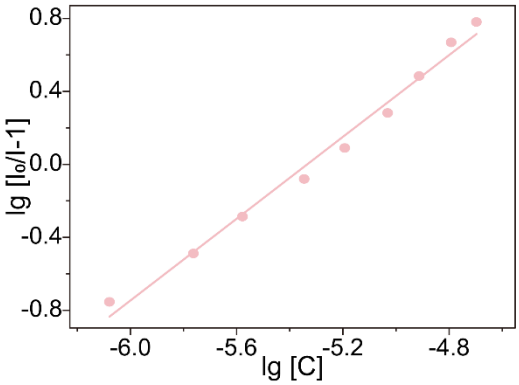

Fig. S12. KSV plot of RhB@Tb-BPDC toward DTZ by monitoring 545 nm.

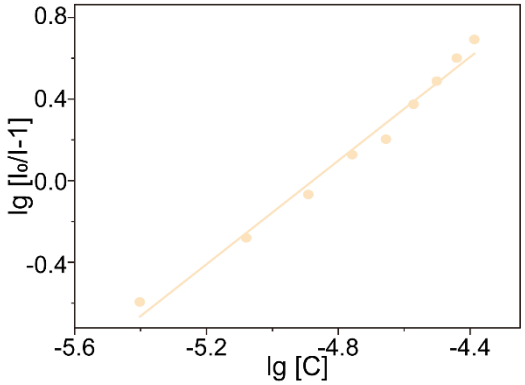

Fig. S13. KSV plot of RhB@Tb-BPDC toward ODZ by monitoring 545 nm

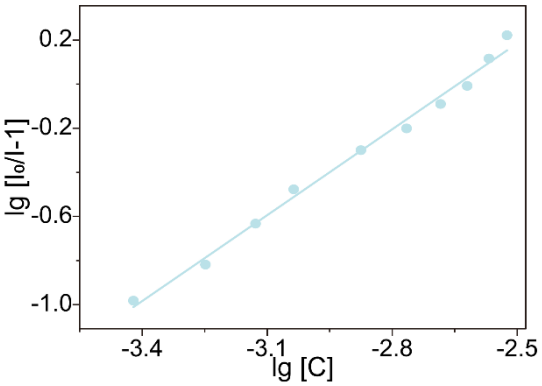

Fig. S14. KSV plot of RhB@Tb-BPDC toward NFZ by monitoring 545 nm

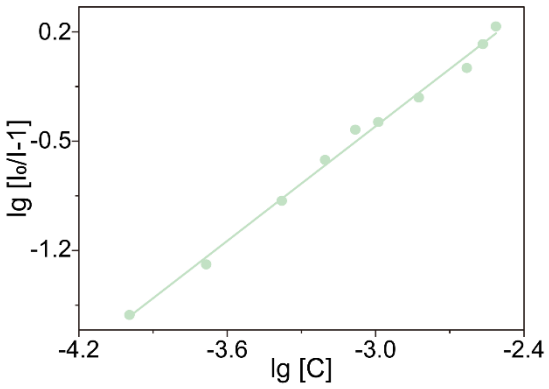

Fig. S15. KSV plot of RhB@Tb-BPDC toward NFT by monitoring 545 nm.

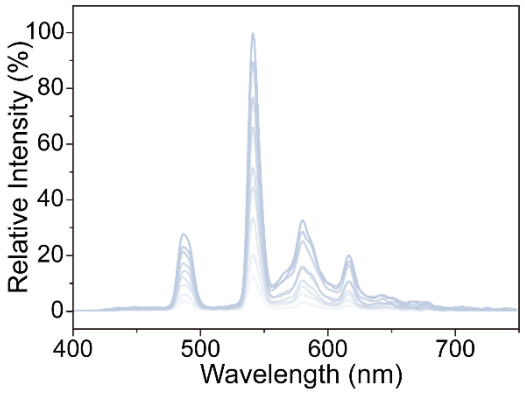

Fig. S16. Concentration dependence between RhB@Tb-BPDC and DTZ in the presence of NFZ.

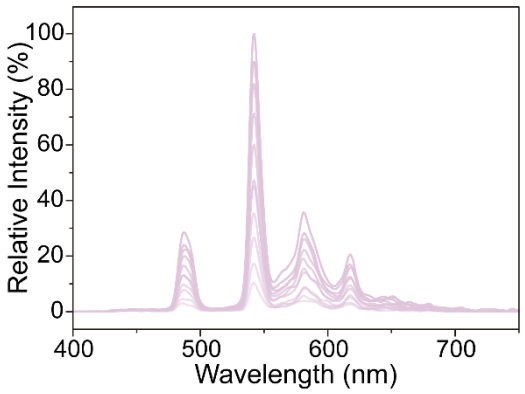

Fig. S17. Concentration dependence between RhB@Tb-BPDC and ODZ in the presence of NFZ.

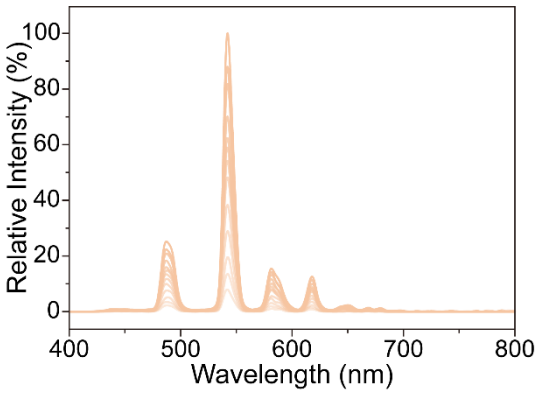

Fig. S18. Concentration dependence between Tb-BPDC and DTZ.

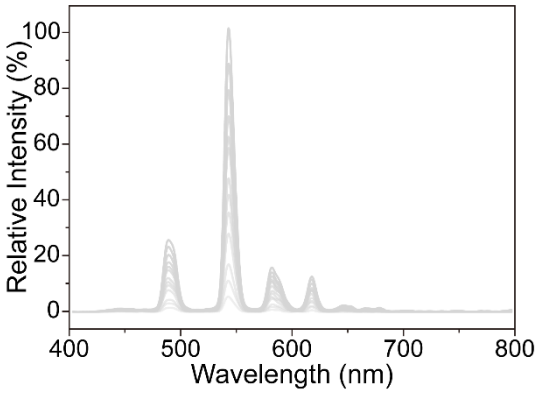

Fig. S19. Concentration dependence between Tb-BPDC and ODZ.

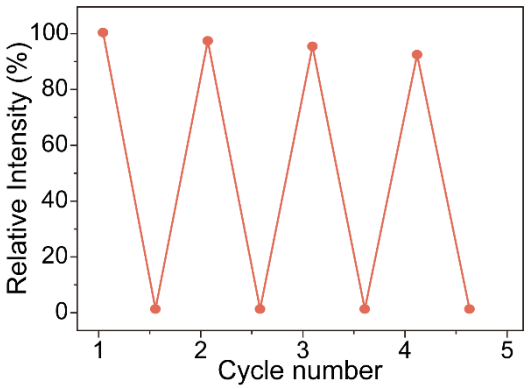

Fig. S20. Recyclability of the sensor toward DTZ and ODZ in water.

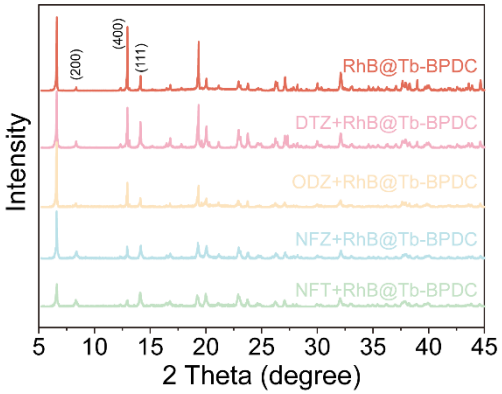

Fig. S21. PXRD patterns of RhB@Tb-BPDC before and after detecting DTZ, ODZ, NFT and NFZ.

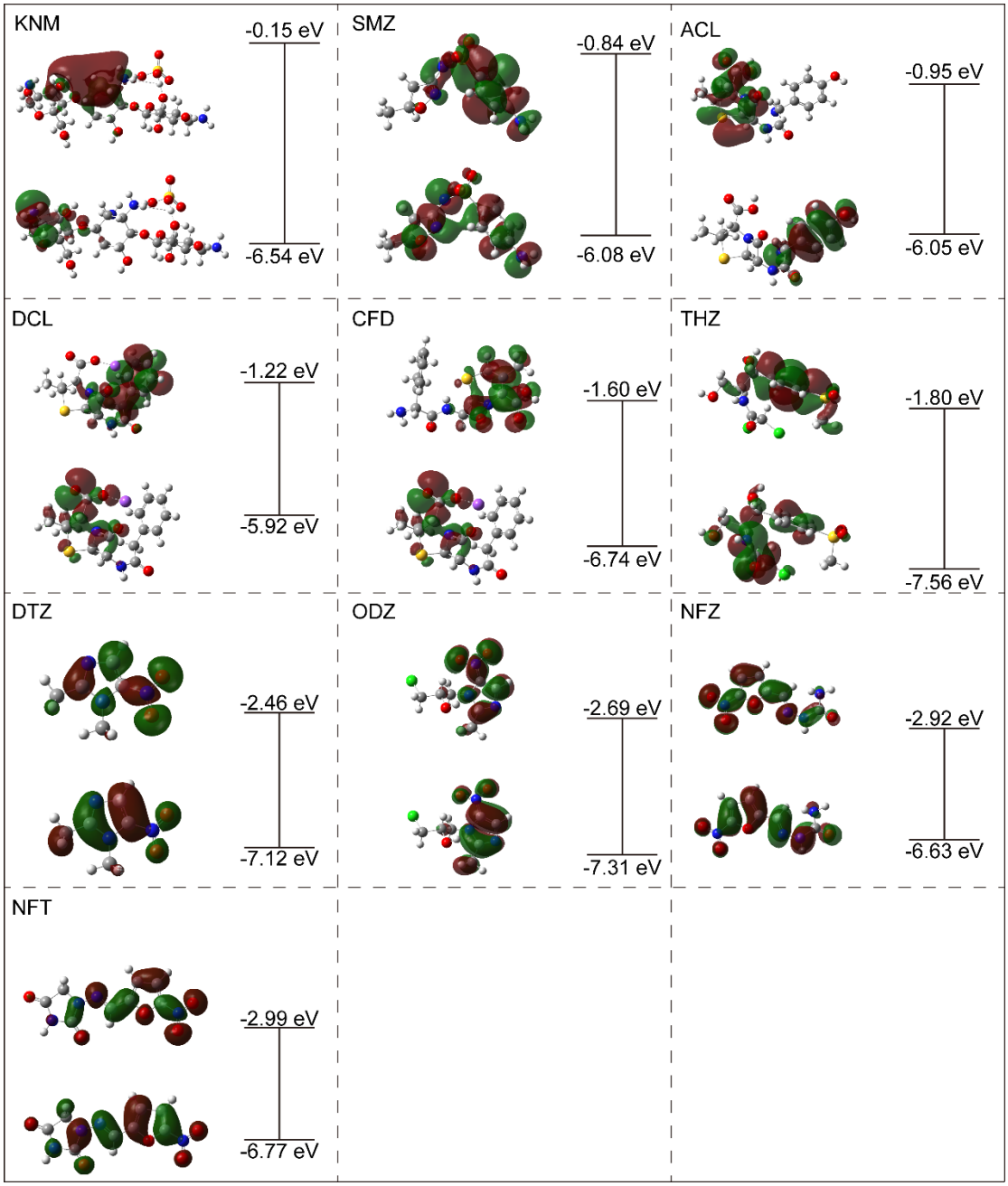

Fig. S22. The values and frontier molecular orbitals of HOMO and LUMO energy levels of antibiotics.

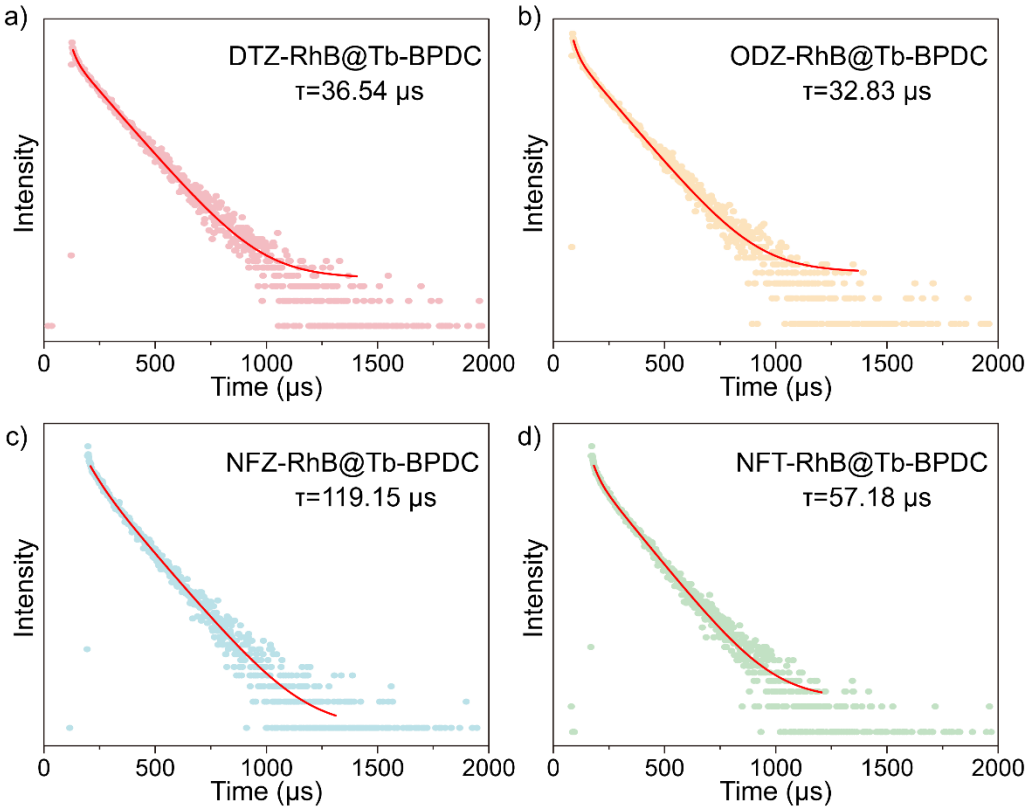

Fig. S23. Luminescent lifetimes of DTZ-RhB@Tb-BPDC, ODZ-RhB@Tb-BPDC, NFZ-RhB@Tb-BPDC, and NFT-RhB@Tb-BPDC.

2.4. Stability and Biotoxicity

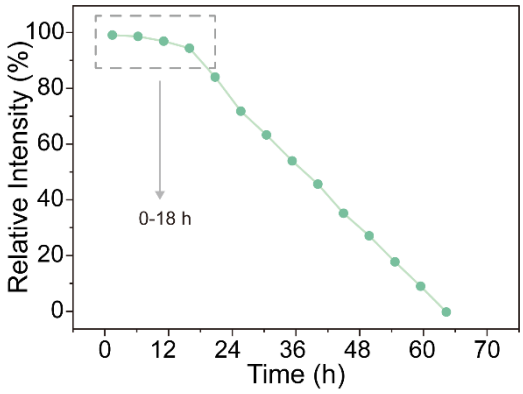

Fig. S24. Relationship between luminescence intensity at 545 nm and time.

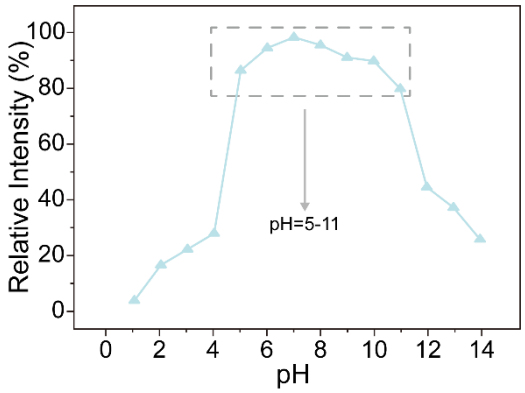

Fig. S25. Relationship between luminescence intensity at 545 nm and pH values.

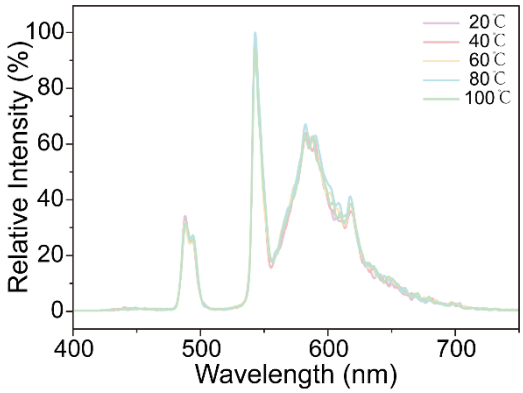

Fig. S26. Temperature-dependent photoluminescence spectra of RhB@Tb-BPDC.

In the exploration of the potential utility of RhB@Tb-BPDC composite materials as sensors for the detection of antibiotics in aqueous solutions, a thorough assessment of their stability within aqueous phases was undertaken. Given the intricate nature of real-world application environments, it was deemed imperative to evaluate the material's stability under conditions simulating natural aquatic environments. To this end, finely ground samples of RhB@Tb-BPDC were uniformly suspended in deionized water to establish a simulated aqueous environment. To ensure homogeneous dispersion of the samples and to replicate the dynamic conditions prevalent in practical applications, the suspension was subjected to continuous stirring at ambient temperature for a duration of 30 minutes. Subsequently, a systematic evaluation of the material's stability was conducted by measuring the fluorescence intensity of the suspension at predetermined time points and comparing it with the initial intensity. Over an observation period of 18 hours, RhB@Tb-BPDC exhibited remarkable stability, maintaining more than 80% of its initial fluorescence intensity, which underscores its exceptional resistance to photobleaching. Furthermore, considering the potential impact of environmental pH fluctuations on material performance, the fluorescence stability of RhB@Tb-BPDC was assessed across a broad pH spectrum ranging from 1 to 14. The findings indicated that RhB@Tb-BPDC maintained commendable fluorescence stability within the pH range of 5 to 11, thus demonstrating its considerable resilience to pH variances. Acknowledging that temperature fluctuations are a commonplace environmental parameter in natural water bodies, the influence of temperature variations on the stability of RhB@Tb-BPDC was further scrutinized. Through experiments simulating various thermal conditions, the material manifested a robust resistance to temperature fluctuations, with its fluorescence characteristics remaining substantially unaffected. This lays a robust foundation for its applicability across diverse climatic conditions.In summary, these comprehensive experimental outcomes not only affirm the exceptional stability of RhB@Tb-BPDC in aqueous environments but also accentuate its substantial potential for applications in chemical and biological sensing within aqueous solutions. These insights pave the way for the deployment of RhB@Tb-BPDC in environmental monitoring and pollutant detection realms, heralding its pivotal role in future water quality monitoring technologies.

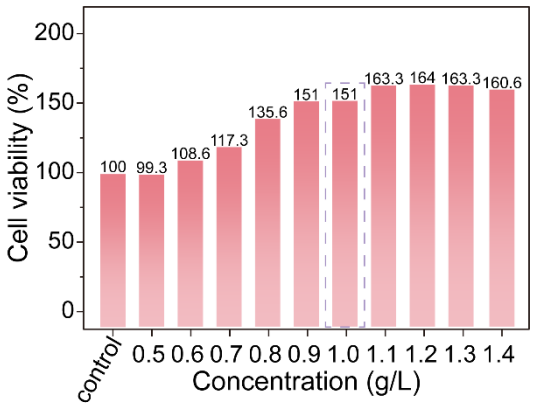

Fig. S27. Cytotoxicity Assay of RhB@Tb-BPDC.

In the context of evaluating the RhB@Tb-BPDC composite material for its potential application in real-world detection scenarios and environmental monitoring, an exhaustive investigation into its toxicological profile was conducted. Given the critical importance of material safety for both in vitro and in vivo applications, a rigorous series of cytotoxicity assessments were systematically executed. The initial phase involved subjecting RhB@Tb-BPDC samples to standardized cytotoxicity assays to emulate biological environments, aiming to rigorously evaluate the biocompatibility of the material across various concentrations and exposure durations. The outcomes of the cytotoxicity assays indicated a notable absence of cytotoxic effects within a wide concentration spectrum of RhB@Tb-BPDC, with cell viability rates consistently exceeding the thresholds established for biocompatible materials. Such results underscore the minimal toxicological impact of RhB@Tb-BPDC, bolstering its candidacy for safe incorporation in diverse biomedical and environmental applications. These insights underscore RhB@Tb-BPDC's favorable toxicological characteristics, reinforcing its viability for deployment in various applications, including environmental monitoring and real-time detection systems. The integration of RhB@Tb-BPDC's low toxicity with its demonstrated stability in aqueous environments highlights its considerable promise as a material for antibiotic detection, paving the way for its future application in advanced sensing technologies and environmental conservation efforts.

Table S1 Quantum yield of Tb-BPDC with varying RhB content.

Materials	1	2	3	4	5	average
Tb-BPDC	22.85	25.77	25.03	23.33	24.57	24.31
$RhB_{0.2}$@ Tb- BPDC	28.74	29.05	32.80	33.43	32.18	31.24
$RhB_{0.4}$@ Tb- BPDC	26.28	27.03	23.53	25.75	22.56	25.03
$RhB_{0.6}$@ Tb- BPDC	26.44	26.67	22.95	24.21	24.48	24.95
$RhB_{0.8}$@ Tb- BPDC	24.67	21.88	22.58	24.44	22.83	23.28
$RhB_{1.0}$@ Tb- BPDC	19.92	21.18	22.33	22.76	21.16	21.47

Table S2 Literature research on the detection limit of ODZ and DTZ

Detect method	Antibiotics	LOD (μ mol/L)	Ref.
Luminescence detection	ODZ	0.15	4
Luminescence detection	ODZ	5.0	5
Luminescence detection	ODZ	0.52	6
Luminescence detection	ODZ	0.319	7
Luminescence detection	ODZ	0.171	8
Luminescence detection	DTZ	20	9
electrochemical	DTZ	0.021	10
electrochemical	DTZ	0.00178	11
electrochemical	ODZ	0.0072	12
electrochemical	ODZ	0.021	13
photonic crystal sensors	ODZ	0.050	14
electrochemical	ODZ	0.059	15
electrochemical	ODZ	0.003	16
electrochemical	ODZ	0.000845	17
electrochemical	ODZ	0.009	18
electrochemical	ODZ	8.7	19
electrochemical	DTZ	0.0034	20
electrochemical	DTZ	0.0060	21
electrochemical	DTZ	0.0020	22
electrochemical	DTZ	0.0036	23
Luminescence detection	DTZ	0.00073	24
Luminescence detection	ODZ	0.00046	24
Fluorescence detection	ODZ	0.32	25
Luminescence detection	DTZ	230	26
Luminescence detection	ODZ	90	26
Luminescence detection	ODZ	0.8	27
Luminescence detection	ODZ	0.63	28
Luminescence detection	DTZ	0.004	29

Luminescence detection	DTZ	0.012	30
Luminescence detection	DTZ	30.66	31
Luminescence detection	DTZ	0.09	32
Luminescence detection	DTZ	2.9	33
Luminescence detection	ODZ	0.00598	This work
Luminescence detection	DTZ	0.0108	This work

3. Reference

1. G. Accorsi, N. Armaroli, A. Parisini, M. Meneghetti, R. Marega, M. Prato and D. Bonifazi, *Adv. Funct. Mater.*, 2007, **17**, 2975–2982.
2. H. N. Abdelhamid, Z. Huang, A. M. El-Zohry, H. Zheng and X. Zou, *Inorg. Chem.*, 2017, **56**, 9139–9146.
3. M.-L. Shen, B. Liu, L. Xu and H. Jiao, *J. Mater. Chem. C*, 2020, **8**, 4392-4400.
4. X. Gao, N. Chen, M. Cao, Y. Shi and Q. Zhang, *Chin. J. Struct. Chem.*, 2022, **41**, 2211110-2211116.
5. B.-X. Dong, Y.-M. Pan, W.-L. Liu and Y.-L. Teng, *Cryst. Growth Des.*, 2018, **18**, 431-440.
6. B. Li, Y.-Y. Jiang, Y.-Y. Sun, Y.-J. Wang, M.-L. Han, Y.-P. Wu, L.-F. Ma and D.-S. Li, *Dalton Trans.*, 2020, **49**, 14854-14862.
7. J.-M. Li, R. Huo, X. Li and H.-L. Sun, *Inorg. Chem.*, 2019, **58**, 9855-9865.
8. J.-H. Wei, J.-W. Yi, M.-L. Han, B. Li, S. Liu, Y.-P. Wu, L.-F. Ma and D.-S. Li, *Chem.-Asian J.*, 2019, **14**, 3694-3701.
9. Y. Sun, B.-X. Dong and W.-L. Liu, *Spectrochimica Acta Part a-Molecular and Biomolecular Spectroscopy*, 2019, **223**, e117283.
10. C. Karuppiah, S. M. Babulal, T.-W. Chen, S.-M. Chen, L.-F. Hsu, D. A. A. Farraj, S. K. Ramaraj, M. S. Elshikh and C.-C. Yang, *J. Environ. Chem. Eng.*, 2022, **10**, e108227.
11. K. Behera, B. Mutharani, Y.-H. Chang, M. Kumari and F.-C. Chiu, *Polymers*, 2024, **16**, e162.
12. J. Ganesamurthi, X.-R. Chen, R.-S. Juang, S. Y. Wei and D. Y. Lin, *J. Ind. Eng. Chem.*, 2023, **127**, 270-282.
13. X. Niu, J. Yang and J.-F. Ma, *Sens. Actuator B-Chem.*, 2023, **387**, e133819.
14. Z. He, J. Liu, C. Zhang, Y. Sun, Q. Chen, J. Zhang, S. Liu, C. Yue, M. Ye and K. Zhang, *Anal. Bioanal. Chem.*, 2023, **415**, 4221-4232.
15. C. Koventhan, V. Vinothkumar and S.-M. Chen, *New J. Chem.*, 2021, **45**, 12593-12605.
16. B. Muthukutty, A. Krishnapandi and S.-M. Chen, *New J. Chem.*, 2020, **44**, 2489-2499.
17. K. Venkatesh, R. Rajakumaran, S.-M. Chen, C. Karuppiah, C.-C. Yang, S. K. Ramaraj, M. A. Ali, F. M. A. Al-Hemaid, M. S. El-Shikh and B. M. A. Almunqedhi, *Chemosphere*, 2021, **273**, e129665.
18. G. Kesavan, V. Vinothkumar and S.-M. Chen, *J. Alloy. Compd.,* 2021, **867**, e159019.
19. H. Wang, X. Bo, M. Zhou and L. Guo, *Anal. Chim. Acta*, 2020, **1109**, 1-8.
20. N. M. Umesh, J. A. Jesila, S.-F. Wang, K. S. S. Devi, M. Govindasamy, A. A. Alothman and R. A. Alshgari, *Colloid Surf. B-Biointerfaces*, 2021, **200**, e 111577.

21. R. Rajakumaran, K. Balamurugan, S.-M. Chen and R. Sukanya, *Anal. Chim. Acta*, 2022, **1190**, e339234.
22. S. V. Selvi, U. Rajaji, S.-M. Chen and J. N. Jebaranjitham, *Colloid Surf. A-Physicochem. Eng. Asp.*, 2021, **631**, e127733.
23. X. Ma, J. Li, J. Luo, C. Liu and S. Li, *Anal. Methods*, 2018, **10**, 3380-3385.
24. X. Ji, S. Wu, D. Song, S. Chen, Q. Chen, E. Gao, J. Xu, X. Zhu and M. Zhu, *Appl. Organomet. Chem.*, 2021, **35**, e6359.
25. L.-B. Wang, J.-J. Wang, E.-L. Yue, J.-F. Li, C. Bai, L. Tang, X. Wang, X.-Y. Hou and Y. Zhang, *J. Solid State Chem.*, 2022, **309**, e123026.
26. G. Zhang, J. Cui, H. Zhang, J. Yang, H. Zhang, H. Han and G. Wang, *Inorg. Chem. Commun.*, 2022, **137**, e109173.
27. M.-L. Han, G.-X. Wen, W.-W. Dong, Z.-H. Zhou, Y.-P. Wu, J. Zhao, D.-S. Li, L.-F. Ma and X. Bu, *J. Mater. Chem. C*, 2017, **5**, 8469-8474.
28. S.-L. Sun, X.-Y. Sun, Q. Sun and E.-Q. Gao, *Crystengcomm*, 2021, **23**, 3167-3174.
29. C. Li, F. Zhang, X. Li, G. Zhang and Y. Yang, *J. Lumines.*, 2019, **205**, 23-29.
30. K. Wang, Y. Dong, X. Zhao, K. Duan, R. Zhao, Y. Ye, J. Guo, H. Pan, H. Tang and Y. Ma, *J. Mol. Struct.*, 2023, **1284,** e135458.
31. Y. Gong, J. Li, N. Wang and X. Li, *J. Solid State Chem.*, 2024, **330**, e124485.
32. K. Wang, L. Yang, L. Li, X. Dong, Z. Wang, H. Tang, W. Sun and Y. Ma, *Arab. J. Chem.*, 2022, **15**, e104295.
33. H.-W. Yang, P. Xu, X.-G. Wang, X.-J. Zhao and E.-C. Yang, *Z. Anorg. Allg. Chem.*, 2020, **646**, 23-29.